Journal of
Materials Chemistry A

ROYAL SOCIETY
OF CHEMISTRY

PAPER

View Article Online
View Journal | View Issue

Cite this: *J. Mater. Chem. A*, 2025, **13**, 6513

Enhanced photocatalytic performance for CO_2 reduction *via* an S-scheme heterojunction between perovskite nanocrystals and $BiVO_4$†

I.-Hua Tsai,[a] Yi-Ru Kuo,[a] Hirotsugu Hiramatsu [a] and Eric Wei-Guang Diau *[ab]

Received 10th October 2024
Accepted 18th January 2025

DOI: 10.1039/d4ta07216b

rsc.li/materials-a

This study presents the successful synthesis of an S-scheme heterojunction between aged $Cs_{0.5}FA_{0.5}PbBr_3$ (CF) perovskite nanocrystals and a $BiVO_4$ semiconductor, aiming to enhance the photocatalytic CO_2 reduction performance. Through meticulous optimization of synthetic methods, material ratios, and the pH of $BiVO_4$, we achieved a remarkable CO production yield of 865 ± 38 μmol g^{-1} in 12 h when the CF to $BiVO_4$ ratio was 15 : 1 and the pH value of the synthesized $BiVO_4$ was adjusted to 4; the individual CF and $BiVO_4$ photocatalysts can only produce CO with yields of 270 and 71 μmol g^{-1}, respectively. Characterization techniques including XRD, SEM-EDS, PL, TCSPC, and UPS spectroscopy confirmed the formation of the S-scheme heterostructure and enhanced photocatalytic performance in varied proportions of CF *versus* $BiVO_4$. The S-scheme heterojunction photocatalyst effectively inhibited electron–hole recombination, facilitating enhanced charge separation and electron–hole transfer for efficient photocatalytic CO_2 reduction. This research not only rejuvenated the photocatalytic capabilities of aged perovskite materials but also addressed the critical challenge of formation of an S-scheme heterojunction between CF and $BiVO_4$, offering a promising pathway for future design of efficient photocatalysts for CO_2 reduction.

Introduction

Artificial photosynthesis technology rapidly became a pivotal implement in scientific research and industrial applications.[1–5] By manipulating light to induce, catalyze, and control chemical reactions, this technique offered a novel and effective approach to photochemical synthesis. Artificial photosynthesis enhanced both the rate and selectivity of photocatalytic reactions, reducing energy consumption and minimizing by-product formation, thus making it a prominent topic in green chemistry and sustainable development. Moreover, with the rapid advancement of photocatalytic materials, the prospects for applications of artificial photosynthesis in medicine, materials science, and environmental protection expanded significantly.[6,7] However, the mechanistic challenges of CO_2 reduction in artificial photosynthesis remain significant. Efficient charge separation, electron selectivity and long-term stability of photocatalysts are crucial yet challenging to achieve.[8–10] The S-scheme heterojunction offers a promising solution by leveraging its unique ability to enhance charge separation *via* an internal electric field while preserving high-energy charge carriers for effective catalytic reactions.[11,12] This approach directly addresses the inherent limitations of traditional photocatalytic systems, making it a compelling strategy for artificial photosynthesis.

Of particular interest was the widespread attention garnered by the application of perovskite materials in artificial photosynthesis. Perovskite materials exhibited excellent light absorption properties, efficient separation of photogenerated electron–hole pairs, and good chemical stability, rendering them highly promising photocatalysts.[13–17] In recent years, perovskite materials have demonstrated outstanding performance in visible light-driven photocatalytic reactions, not only enhancing reaction rates but also significantly improving product selectivity.[18–20]

However, despite their immense potential in the field of photocatalysis, perovskite materials faced several challenges. First, stability issues, particularly under intense light, high humidity, and oxygen-rich conditions, led the perovskite to age and have decreased photocatalytic efficiency.[21–24] Second, the synthesis of perovskite materials often involved the use of toxic solvents, posing potential threats to the environment and human health.[25,26] Furthermore, preparation methods for lead-based perovskites, such as hot-injection and ligand-assisted

---

[a] *Department of Applied Chemistry, Institute of Molecular Science, National Yang Ming Chiao Tung University, 1001 Ta-Hseuh Rd, Hsinchu 300093, Taiwan. E-mail: diau@nycu.edu.tw*

[b] *Center for Emergent Functional Matter Science, National Yang Ming Chiao Tung University, 1001 Ta-Hseuh Rd, Hsinchu 300093, Taiwan*

† Electronic supplementary information (ESI) available: Experimental methods, supplementary figures and tables for SEM, SEM-EDS, UPS, PL, and TCSPC and a summary of comparison of this work with the others using the heterojunction catalyst for photocatalytic applications. See DOI: **https://doi.org/10.1039/d4ta07216b**

reprecipitation methods, suffered from batch-to-batch inconsistency and poor reproducibility, posing challenges for large-scale applications.[27–34] Additionally, structural defects and interface instability in aged perovskite materials adversely affected their photocatalytic performance. Defects within the crystal structure could act as recombination centers for electron–hole pairs, thereby reducing photocatalytic performance. Interface instability issues hindered efficient charge transfer between perovskite materials and other components, limiting their photocatalytic activity.[35–39] Moreover, despite the efforts to maintain environmental conditions, fresh perovskite materials were prone to phase transitions over time, resulting in significant declines in their photocatalytic efficiency. This instability remained a critical factor preventing the widespread and long-term application of perovskite materials in photocatalytic CO_2 reduction.[40–43] In the context of aged perovskites, the formation of an S-scheme heterojunction with complementary semiconductor materials presents a dual benefit: stabilizing the material while simultaneously enhancing its photocatalytic activity. Aging processes often induce structural and electronic changes, such as increased defect density, which can act as recombination centers for charge carriers. The built-in electric field of the S-scheme heterojunction mitigates this issue by directing the migration of high-energy electrons and holes to separate surfaces, thereby reducing recombination rates and maximizing charge carrier availability. To address these issues, researchers began exploring methods to optimize perovskite materials by forming S-scheme heterojunctions. One effective strategy involved using bismuth materials such as $BiVO_4$, Bi_2WO_6, BiOI, BiOBr and so on.[44–51] $BiVO_4$ exhibited excellent photocatalytic performance, especially in the visible light range, owing to its strong light absorption capabilities. When combined with perovskite materials, $BiVO_4$ formed heterostructures that effectively enhanced the charge separation efficiency of photogenerated electron–hole pairs, thereby improving photocatalytic performance.[52–57]

$BiVO_4$ offered several advantages: first, it possessed higher chemical stability and resistance to degradation, which protected perovskites from moisture and oxygen interference, thereby enhancing the stability of photocatalytic materials. Second, $BiVO_4$ as a synergistic photocatalyst promoted the separation of photogenerated carriers in perovskite materials, reducing recombination probabilities and enhancing photocatalytic efficiency. From a timescale perspective, the recombination time of photogenerated carriers occurs within picoseconds to nanoseconds, while the oxidation–reduction timescale of carriers generally spans around microseconds. Reducing the recombination rate of carriers minimizes the loss of energy through non-productive pathways, thereby increasing the availability of carriers to participate in the redox reactions required for photocatalysis. Enhanced carrier efficiency directly contributes to improved photocatalytic activity, thereby facilitating a faster and more efficient conversion of CO_2 into useful products.[58,59] Third, $BiVO_4$ was non-toxic and environmentally friendly, mitigating potential hazards associated with lead in perovskite materials and enhancing the material's eco-friendliness.

Numerous studies have reported the enhancement of photocatalytic efficiency through S-scheme heterojunctions, where two semiconductor materials form a junction *via* electrostatic interactions. The primary purpose of such a junction is to suppress carrier recombination within the materials. The internal electric field established through the contact between the materials facilitates carrier recombination at the junction while allowing high-energy electrons and holes to diffuse to the material surface, achieving charge separation and thereby enhancing photocatalytic performance. According to our previous research, a composite of fresh $Cs_{0.5}FA_{0.5}PbBr_3$ (CF) perovskite and BiOI nanosheets was investigated.[60] However, the CO_2 reduction photocatalytic efficiency of the heterojunction materials did not improve. Based on fs-transient absorption spectroscopy (fs-TAS) evidence, although the heterojunction materials exhibited rapid carrier recombination (from 100 and 900 ps decreased to 1 and 35 ps), the intrinsic defects (Bi^{3+} deep traps) in the Bi material led to rapid carrier relaxation, ultimately reducing the photocatalytic activity for CO_2 reduction. Therefore, selecting appropriate bismuth materials remains a critical issue.

In this study, aged $Cs_{0.5}FA_{0.5}PbBr_3$ (CF) perovskites were obtained through a simple stirring process at room temperature over three days, without relying on additional physical (*e.g.*, ultrasonication) or chemical (*e.g.*, oxidizers) methods. $BiVO_4$ was strategically selected as a co-catalyst to form an S-scheme heterojunction with these aged perovskites, owing to its excellent light absorption, chemical stability, and ability to complement the aged perovskite's electronic properties.[61–64] The resulting heterojunction facilitates efficient charge carrier separation and reduces recombination, addressing the intrinsic issues caused by perovskite aging, such as increased defect density and reduced catalytic efficiency. This study not only demonstrates the rejuvenation of aged perovskites *via* the S-scheme heterojunction but also highlights the potential of leveraging aging-induced structural changes to enhance photocatalytic performance, achieving significantly improved CO_2 reduction efficiency.

Results and discussion

CF and $BiVO_4$ materials were synthesized according to the procedures reported elsewhere.[33,57] The synthetic procedures of CF and $BiVO_4$, along with the scheme for photocatalytic CO_2 reduction experiments, are presented in Fig. S1–S3,† respectively. The S-scheme heterojunction structures were prepared for the CF/$BiVO_4$ ratios of 5/1 (CB5-1), 10/1 (CB10-1), 15/1 (CB15-1) and 20/1 (CB20-1) and characterized by varied methods detailed below. X-ray diffraction (XRD) analysis (Fig. 1a) revealed significant changes in the CF perovskite synthesized *via* the hot-addition method after being stirred at room temperature for three days. The freshly synthesized CF perovskite (CF-fresh) exhibited prominent diffraction peaks at angles (2θ) around 15° and 30°, indicative of the orthorhombic phase, as reported in the literature.[65] However, after stirring for three days, new diffraction peaks corresponding to the cubic phase of perovskite appeared. These results suggested that the CF

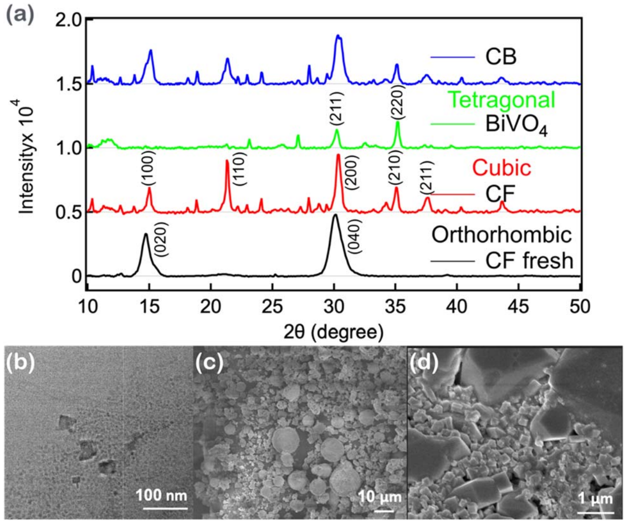

Fig. 1 The crystal phase, crystal structure, and sample morphology of CF, BiVO$_4$, and their heterostructure CB15-1. (a) X-ray diffraction (XRD) spectra, with Bragg's angle peak positions corresponding to literature data for orthorhombic CF, cubic CF, and tetragonal BiVO$_4$; (b) transmission electron microscope (TEM) image of aged CF perovskite nanocrystals; (c) scanning electron microscope (SEM) image of BiVO$_4$ and (d) SEM image of CB15-1.

perovskite underwent a phase transition from the orthorhombic to the cubic phase during the room-temperature stirring process, a common aging phenomenon in many perovskite materials.[66–68]

The Scherrer equation was employed to estimate the crystallite sizes of the fresh and aged CF perovskites in Table S1.†[69,70] The diffraction peaks at (040) for the fresh CF (orthorhombic phase) and (200) for the aged CF (cubic phase) were fitted, yielding crystallite sizes of 7.4 ± 0.1 nm and 17.8 ± 0.6 nm, respectively. The results indicated that the aged CF perovskite aggregated into crystals more than twice the size of the fresh perovskite, likely due to a process similar to Ostwald ripening, which is common in quantum dots.[71–73] This thermodynamically driven process occurs because larger crystals are energetically more stable than smaller ones. As a result, the average size of nanocrystals in the solution increased over time, eventually forming large spherical particles to minimize the total surface area, a phenomenon known as Ostwald ripening. The CF perovskite in this study was subject to such ripening effects. Due to these factors, aged perovskites are generally unsuitable for photocatalytic reactions. The decrease in specific surface area reduces the contact area between reactants and the catalyst, and the aggregation of crystals leads to a loss of active sites, resulting in poor charge separation efficiency and diminished photocatalytic activity. Thus, fresh perovskites typically exhibit better photocatalytic performance than the aged ones. The photocatalytic efficiency would be mentioned in the photocatalysis of CO$_2$ reduction reaction part later. Interestingly, the incorporation of BiVO$_4$ to form an S-scheme heterojunction partially reverses the negative effects of crystal growth in aged CF perovskites. Upon forming the heterojunction, the crystallite size of the composite material (aged CF/BiVO$_4$, CB15-1) decreases to 11.1 nm, suggesting that BiVO$_4$ mitigates the aggregation effects of aged CF. This synergistic interaction between aged perovskites and BiVO$_4$ underscores the ability of S-scheme heterojunctions to exploit structural changes in aged CF that would typically hinder performance, transforming these changes into advantages for photocatalytic CO$_2$ reduction. This improvement likely contributes to an increase in the specific surface area and restoration of active sites, addressing a critical limitation of aged perovskites. By enhancing charge carrier separation, the S-scheme heterojunction effectively rejuvenates the aged perovskites, unlocking their full catalytic potential for sustainable CO$_2$ conversion.

By integrating aged CF with tetragonal phase BiVO$_4$ (ref. 74) through a stirring method, XRD analysis showed that the heterojunction material maintained the crystalline phases of CF and BiVO$_4$, without the appearance of significant impurities or new phases. Interestingly, fitting the diffraction peaks at similar positions for the heterojunction between aged CF and BiVO$_4$ using the Scherrer equation yielded a crystallite size of 11.1 ± 0.3 nm. This indicated that the formation of heterojunctions helped mitigate Ostwald ripening. The presence of BiVO$_4$ likely provided a stabilizing influence, maintaining the perovskite's structural integrity and preserving its surface area, thereby enhancing its photocatalytic activity.

The morphology and size of the materials were examined using scanning electron microscopy (SEM) and transmission electron microscopy (TEM). The TEM image (Fig. 1b) of the CF perovskite after three days of stirring at room temperature revealed that it maintained a highly regular cubic structure on the nanoscale, with most CF perovskite crystals measuring approximately ∼10 nm in size. However, some larger aggregates with a size of around 30 nm were also observed, which aligns with the aging and aggregation phenomena previously detected in the XRD analysis. In this study, certain limitations were encountered during the imaging of the aged CF nanocrystals. Initial attempts to capture high-resolution TEM images (Fig. 1b) to investigate the morphology and crystallinity of the aged CF perovskites resulted in blurred images. This issue arose due to the degradation of the aged CF material under high-energy electron beam exposure in the TEM. Specifically, the initially well-defined rectangular or cubic crystals of the aged CF perovskites became indistinct, likely due to further structural degradation induced by the high-energy electron beam. Such degradation, or potential material decomposition, occurred under the high-energy conditions required for TEM, making it challenging to capture clear structural details at higher magnifications. As a result, SEM was employed, which requires lower energy electron beams and does not involve transmission of electrons through the sample. The lower energy allowed for clearer imaging of the aged CF perovskites without causing further degradation.

For BiVO$_4$, the SEM image (Fig. 1c) showed particle sizes primarily around 1 μm, with some spherical particles approaching 10 μm. These spherical structures are consistent with those reported in the literature using hydrothermal synthetic methods.[75] The SEM images of the heterojunction material CB (Fig. 1d) revealed numerous cubic crystals embedded within an irregularly shaped matrix. The distinctly observable cubic structures were identified as CF perovskite, while some of the irregularly mixed structures were identified as spherical $BiVO_4$. These images indicated that the micron-sized $BiVO_4$ particles and the nanoscale CF perovskite crystals effectively adhered to each other through the stirring method. The morphological observations suggest that the combination of $BiVO_4$ and CF perovskite *via* the stirring method facilitates the formation of a robust heterostructure, enhancing their interaction and integration. This structural integration likely contributes to improved charge transfer efficiency and stability, crucial for enhanced photocatalytic performance.

To confirm the successful composition of the heterojunction material through the stirring method, SEM-EDS was employed to analyze the elemental composition and ratios of CF, $BiVO_4$, and the heterostructure. As shown in Fig. 2, the SEM images, elemental ratios, and elemental mapping for CF perovskite, $BiVO_4$, and the heterojunction materials, respectively, were generated using SEM-EDS. The SEM images of the CF perovskite (Fig. S4†) revealed that most nanocrystals were tightly packed, forming smooth surfaces, but some crystal sizes reached the μm scale. Elemental scanning of both the smooth surface and micron-sized crystals indicated that the elemental ratios of Cs, Pb, and Br were 19.23%, 16.04%, and 64.73%, respectively. Typically, the stoichiometric chemical formula for perovskites is ABX_3, implying a Pb : Br ratio of 1 : 3. In this case, the CF perovskite exhibited a Pb : Br ratio of 1 : 4 after three days of stirring at room temperature, consistent with the results reported elsewhere.[76,77] This result suggests that no halide vacancies were formed in the Br-rich CF perovskite after three days of stirring, which is crucial as halide vacancies can lead to ion migration and eventual structural degradation of the perovskites. The presence of micron-sized crystals observed in the SEM images further corroborated the aggregation due to aging. The morphology of $BiVO_4$ (Fig. S5†) appeared as cotton-like spherical structures, with elemental ratios of Bi, V, and O being 13.17%, 8.68%, and 78.16%, respectively. The deviations from the chemical stoichiometry might be attributed to the vanadium vacancies that existed in $BiVO_4$.[78] In the CF/$BiVO_4$ heterostructure (Fig. 2), SEM-EDS images clearly showed the presence of all elements (Cs, Pb, Br, Bi, V, and O), with proportions of 13.71%, 11.52%, 43.29%, 2.56%, 1.32%, and 27.6%, respectively. These elements were uniformly distributed throughout the heterostructure material, and the Pb/Br and V/O

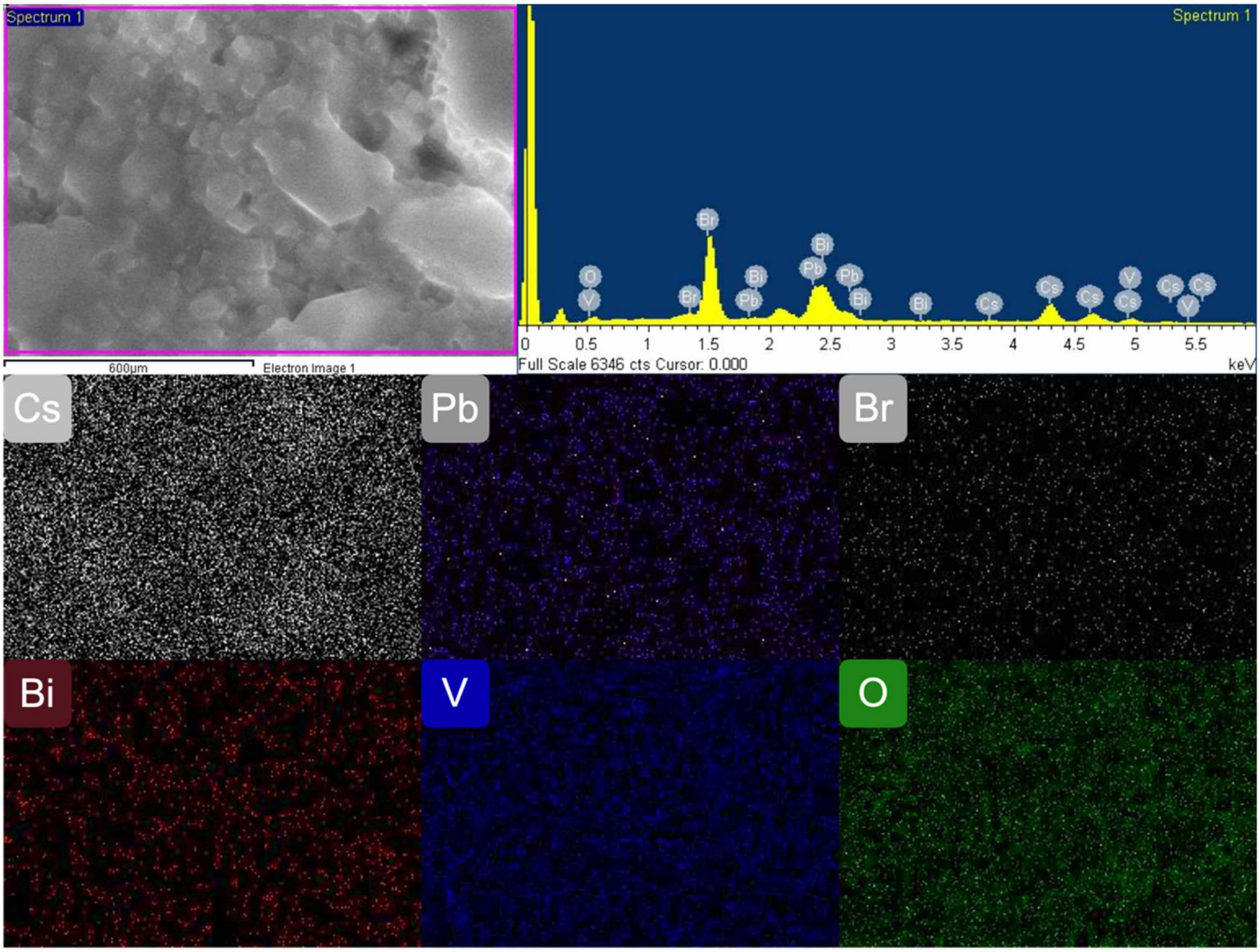

Fig. 2 Distribution and elemental composition of the CF/$BiVO_4$ (CB15-1) heterostructure measured with SEM-EDS. The atomic ratios of Cs, Pb, Br, Bi, V, and O in CB15-1 were 13.71%, 11.52%, 43.29%, 2.56%, 1.32%, and 27.6%, respectively.

ratios were similar to those observed previously. Notably, even though the $BiVO_4$ proportion in the heterojunction material was much lower than that of CF, Bi was still detectable on the material's surface. Moreover, overlapping the elemental mapping of Bi and Pb (Fig. S6†) revealed a high degree of overlap between Bi and Pb atoms, further confirming the successful formation of the heterostructure between the two materials.

The band alignment in heterojunctions is crucial as it determines the type of heterojunction formed and significantly impacts photocatalytic performance. Type II heterojunctions are particularly suitable for photocatalytic systems due to their efficient charge separation and higher redox potentials, which increase the likelihood of carrier participation in redox reactions. Therefore, the optical spectroscopic evidence was used to measure and estimate the band gaps, Fermi levels, valence band maxima (VBM) and conduction band minima (CBM) of individual materials. This allowed the construction of a band alignment diagram and the determination of the heterojunction type.

The steady-state absorption spectra of the individual photocatalysts, CF and $BiVO_4$, were measured in both film and powder forms. As shown in Fig. 3a and b, the steady-state absorption spectra indicated that both CF perovskite (black curve) and $BiVO_4$ (gray curve) exhibited a baseline that increased gradually from 700 nm to 550 nm. This might be attributed to the disordered structure and lattice defects present in the aged CF perovskite, leading to the below band gap absorption, while $BiVO_4$ displayed scattering interference in the powder sample. Tauc plots[79] and the Kubelka–Munk[80] function were used to further estimate the band gaps, revealing band gaps of 2.32 eV for CF and 2.50 eV for $BiVO_4$. Further measurements of the heterojunction material's absorption spectra were conducted. Fig. 3a and b also show the absorption spectra of CF/$BiVO_4$ heterostructure (CB5-1 was the red curve, CB10-1 was the yellow curve, CB15-1 was the green curve, and CB20-1 was the blue curve). Despite the lack of a direct correlation between absorbance intensity and the ratio of heterostructure composition, a spectral shift was observed in the heterostructures compared to CF perovskite after estimating their band gaps from the absorption spectra. However, the spectral shift observed at the heterojunction could be attributed to several possible factors, such as an increase in particle size, ionic migration at the heterojunction interface, or band shifts in the valence band and conduction band due to the formation of the heterostructure. Relying solely on absorption spectra was insufficient to conclusively determine the successful formation of heterostructures. Therefore, additional optical evidence was required to ascertain which proportions of heterostructure materials were most suitable for use in photocatalytic reactions. The band gaps of the composite samples CB5-1, CB10-1, CB15-1, and CB20-1 were estimated from Tauc plots to be 2.42, 2.31, 2.38, and 2.33 eV, respectively.

Photoluminescence (PL) spectroscopy was used to confirm the successful formation of the composite material. When CF perovskite was successfully integrated with another

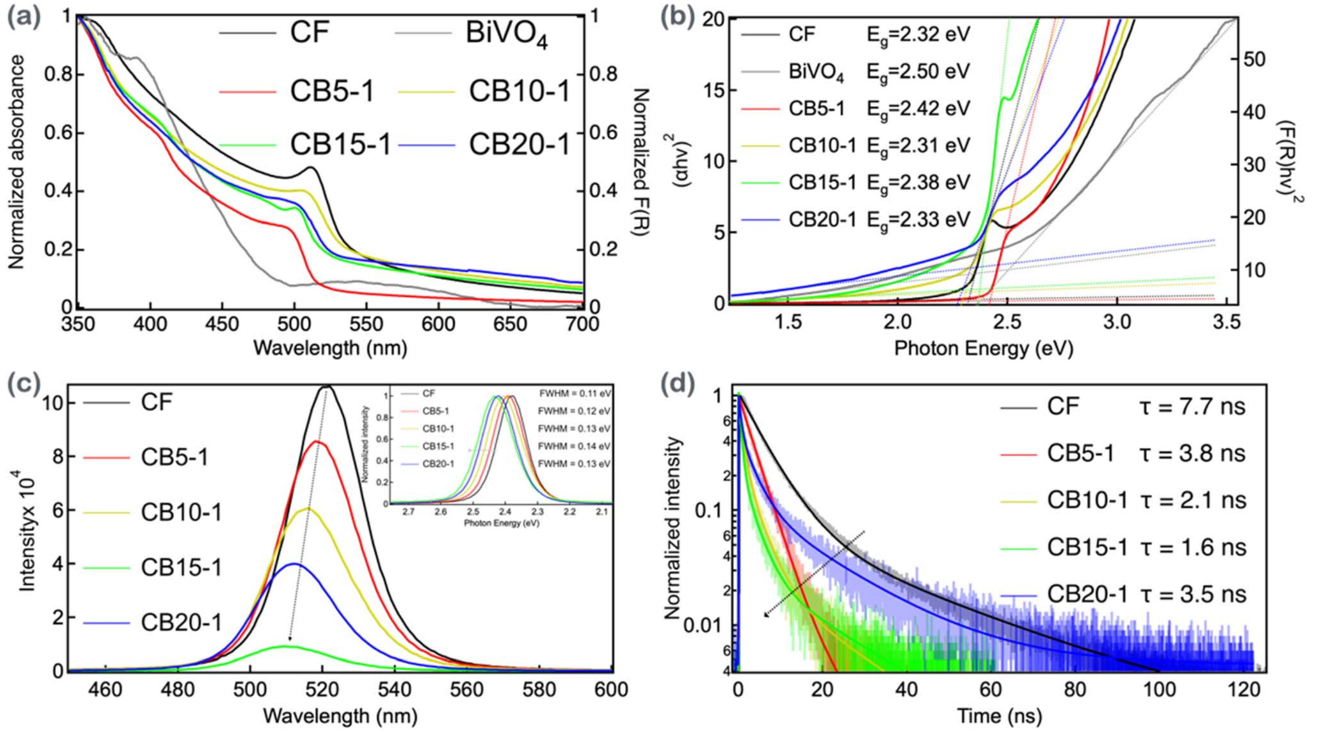

Fig. 3 Optical properties of CF and $BiVO_4$ and their heterojunction materials. (a) Steady state absorption spectra; (b) band gap estimated using the Tauc plot with the band gaps of CF, $BiVO_4$, CB5-1, CB10-1, CB15-1, and CB20-1 shown in the legend; (c) steady state PL spectra with the corresponding PL peak positions and FWHMs shown in the legend and inset, respectively; (d) PL decay profiles with the corresponding average PL lifetimes shown in the legend.

semiconductor material, the fluorescence of CF was quenched due to the inability of photogenerated carriers to recombine radiatively on the energy band of CF. The CF and heterojunction materials was excited at a wavelength of 375 nm, and the emission wavelengths were collected between 450 and 600 nm. The results (Fig. 3c) indicated that with an increasing CF/$BiVO_4$ ratio, the heterojunction materials exhibited fluorescence quenching. Additionally, Gaussian fitting of the PL spectrum profile showed a blue shift of the maximum PL peak from 2.38 eV to 2.43 eV in the heterojunction materials, similar to the results obtained from absorption spectra. The broadening of the PL full width at half maximum (FWHM) also indicated that some defects were formed during the heterojunction process. In the PL spectrum of the CB15-1 heterojunction material, the emission intensity was the weakest with the most blue spectral shift, indicating significant quenching of fluorescence at this ratio, suggesting that it should have the best heterojunction effect for charge separation.

Furthermore, PL decay profiles from Fig. 3d also described the success of heterojunction formation. With an increasing CF/$BiVO_4$ ratio, the fluorescence lifetime of the heterojunction gradually decreased. Fitting the decay profiles using a multi-exponential function revealed that the decay profiles of CF could be described by two time coefficients: 5.8 ns (92%) and 27.9 ns (8%), which could be categorized as free carrier recombination and trap-assisted recombination, respectively.[81,82] These parameters are listed in Table S3† as $\tau_2(A_2)$ and $\tau_3(A_3)$. Similarly, CB5-1 could also be expressed with two time coefficients, 3.6 ns (99%) and 17.6 ns (1%), both of which were significantly faster than the time coefficients of CF, indicating that $BiVO_4$ had the effect of contributing to charge carrier separation.

Interestingly, when the CF/$BiVO_4$ ratio increased compared to those of CB10-1, CB15-1, and CB20-1, three time coefficients were needed for global fitting of the PL temporal profiles. Taking CB15-1 as an example, the three time coefficients are 0.7 ns (82%), 3.6 ns (15%), and 17.6 ns (3%), categorized as heterojunction charge transfer, free carrier recombination, and trap-assisted recombination, respectively.[60] It was evident that the amplitude A_2 dropped sharply from 92% to 15%. In other words, the heterojunction material significantly reduced the free carrier recombination rate of CF perovskite while introducing an additional sub-nanosecond time coefficient (τ_1). Therefore, CB15-1 has the most effective heterojunction ratio for integrating the two materials. Finally, the average fluorescence lifetime showed that CB15-1 had the shortest fluorescence lifetime among all heterojunction materials, at only 1.7 ns. These observations indicated that CB15-1 has the most effective ratio in suppressing the free carrier recombination of CF and promoting charge carrier separation in the heterostructure. The average lifetimes of the heterojunction materials CB5-1, CB10-1, CB15-1, and CB20-1 were estimated to be 3.8, 1.9, 1.7 and 3.6 ns, respectively. The fitting parameters are presented in Table S3.†

Ultraviolet photoelectron spectroscopy (UPS) data are crucial for understanding the work function and valence band information of the materials, which are essential for elucidating their redox potentials. Initially, in this experiment, the binding energy ($E_{\mathrm{b,Au}}$) of the Au standard sample in the UPS spectrum was measured to be −0.0519 eV. Therefore, calibration of the vacuum level standard of the experimental instrument was necessary to obtain reliable data. Subsequently, UPS spectra (Fig. S7†) for CF and $BiVO_4$ materials were measured and divided into two regions for fitting. The first region, the secondary electron cutoff region with high binding energy, was used to determine the material's work function. The second region, the electron onset region with low binding energy (E_b), was used to determine the energy difference between the VBM in semiconductor materials and the material's work function.

In the high binding energy region, a linear function was used to fit the spectral baseline (from 21 eV to 17 eV). Another linear trend line was fitted at the maximum derivative value to determine the secondary electron cutoff energy (E_{cutoff}) at the intersection of these two lines. The E_{cutoff} values for CF and $BiVO_4$ were 16.62 eV and 16.04 eV, respectively. The material work function (Φ) was calculated using the formula $\Phi = h\nu - (E_{\mathrm{cutoff}} - E_{\mathrm{b,Au}})$ yielding work functions of 4.55 eV for CF and 5.13 eV for $BiVO_4$. Based on the difference in work functions, it was further determined that the internal electric field (E_{IEF}) direction in the composite material points from CF to $BiVO_4$, indicating the formation of an S-scheme heterojunction between CF and $BiVO_4$ (Fig. 4).

Next, to estimate the VBM, the intersection of the baseline and the derivative trend line was used as the onset region E_b. For CF and $BiVO_4$, the electron onset region ranged from −1 eV to 4 eV. A trend line was fitted from −1 eV to 0 eV as the baseline, while another trend line was based on the slope change determined using the derivative function. Thus, the E_b values for CF and $BiVO_4$ were determined to be 1.53 eV and 2.00 eV, respectively (Fig. S7†). The VBM values were calculated using the equation VBM = $\Phi + E_\mathrm{b}$, resulting in VBM values of 6.08 eV for CF and 7.13 eV for $BiVO_4$.

To confirm the formation of the S-scheme heterojunction, an energy level diagram was constructed using the work function, VBM, and bandgap before and after composite formation, as shown in Fig. 4. This diagram aligns with the spectral characteristics observed, indicating that the heterojunction effectively suppresses carrier recombination and enhances charge separation, suggesting significant photocatalytic potential. For effective S-scheme heterojunction formation, it is not required that the semiconductors form a p–n junction;[63] a type II configuration alignment of the valence and conduction bands is sufficient. The material acting as the reduction site (whether n-type or p-type) must have a higher work function and conduction band level than the other semiconductor to induce band bending and form the S-scheme junction, as depicted in Fig. 4.

The photocatalytic mechanism of the S-scheme heterojunction formed between the perovskite and $BiVO_4$ involves efficient charge separation and transfer processes facilitated by the internal electric field (E_{IEF}) at the heterojunction interface. Upon light irradiation, electrons in the conduction band (CB) of the perovskite are excited, leaving holes in its valence band (VB). Simultaneously, $BiVO_4$ absorbs light, generating electron–hole pairs. In the S-scheme configuration, electrons in the CB of

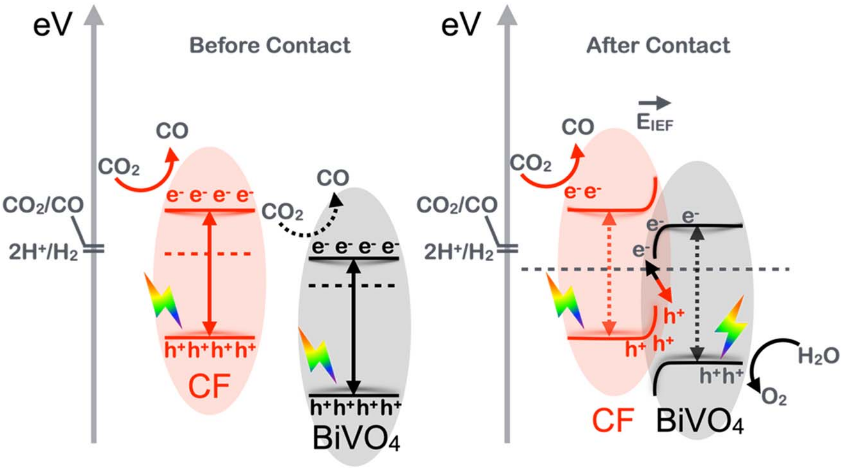

Fig. 4 The energy diagram of CF and $BiVO_4$ to form an S-scheme heterojunction confirmed by the UPS measurements.

$BiVO_4$ recombine with holes in the VB of the perovskite, driven by the built-in electric field. This preserves high-energy electrons in the perovskite's CB and high-energy holes in $BiVO_4$'s VB, which migrate to the surface of their respective materials for CO_2 reduction and water oxidation, respectively. This separation minimizes recombination and maximizes the availability of carriers for the photocatalytic reaction, explaining the observed enhancement in photocatalytic CO_2 reduction performance. The results demonstrated that aged CF could form an S-scheme heterojunction with $BiVO_4$, effectively inhibiting carrier recombination and enhancing charge separation. Photocatalytic CO_2 reduction experiments conducted in a humid environment further verified that the heterostructure could successfully rejuvenate the photocatalytic activity of aged perovskites.

Initially, the photocatalytic CO production yields of individual materials, aged CF perovskite and the $BiVO_4$ semiconductor, were tested under humid conditions. The experimental results showed that the photocatalytic efficiencies of individual CF and $BiVO_4$ were only 270 μmol g^{-1} and 71 μmol g^{-1}, respectively, under one-sun irradiation for 12 h. Both photocatalysts exhibited very low photocatalytic efficiencies under humid conditions. For comparison, photocatalytic experiments were conducted with freshly synthesized and purified CF perovskites under humid conditions. The CO yield after 12 hours was 351 μmol g^{-1}. In contrast, under dry conditions, freshly synthesized CF nanocrystals achieved a significantly higher CO yield of approximately 1100 μmol g^{-1}, as reported in our previous study.[65] This highlights the detrimental effect of water vapor on CF perovskite stability and photocatalytic efficiency. Similarly, $BiVO_4$, despite its strong physicochemical stability in humid environments, did not match the conduction band position with the reduction potential of CO_2, leading to low photocatalytic efficiency. This study aimed to overcome these individual material limitations by combining the two n-type semiconductor materials into an effective heterostructure to achieve higher photocatalytic efficiency.

Two methods were employed to synthesize the heterostructures: the one-pot method and the stirring method. In the first method, pre-dried $BiVO_4$ powder was introduced within the CF perovskite process. The CO_2 photocatalytic reduction results showed that the CO production yield of the heterostructure synthesized by the one-pot method increased to 588 μmol g^{-1}. Compared to the individual materials CF and $BiVO_4$, this represented an increase of over two times and eight times, respectively. This result indicated that the materials did not only add linearly to increase photocatalytic performance but also exhibited a significant synergistic effect, demonstrating that CF and $BiVO_4$ formed an effective heterostructure. Therefore, it was necessary to further optimize the synthesis method of the heterostructure to form more effective heterostructures and improve their photocatalytic performance.

The second method for preparing heterostructures was the stirring method, forming heterostructures through electrostatic interactions between the two materials; the results are shown in Fig. 5a. Different ratios of CF and $BiVO_4$ were tested, including CB5-1, CB10-1, CB15-1, and CB20-1. Photocatalytic performance was evaluated based on CO production yields. The yields for the different heterostructure ratios were 217, 234, 865, and 355 μmol g^{-1} for CB5-1, CB10-1, CB15-1, and CB20-1, respectively. Notably, the heterostructure with a CF to $BiVO_4$ ratio of 15 : 1 exhibited photocatalytic efficiency nearly 1.5 times greater than that obtained by the one-pot method and showed over three times and twelve times the increase compared to the individual materials CF and $BiVO_4$, respectively. This highlighted that the heterostructure formed by the stirring method showed superior photocatalytic performance compared to the one-pot method. It was also observed that when only a low ratio of the composite was used (CB5-1), the heterojunction formation at the material surface involved only a few regions exhibiting the S-scheme. Therefore, a sufficient amount of CF/$BiVO_4$ at a ratio of 15 : 1 was required to effectively facilitate charge carrier recombination and separation, achieving optimized photocatalytic efficiency. On the other hand, when the ratio reached 20 : 1, the excess CF could not form effective S-scheme heterojunctions,

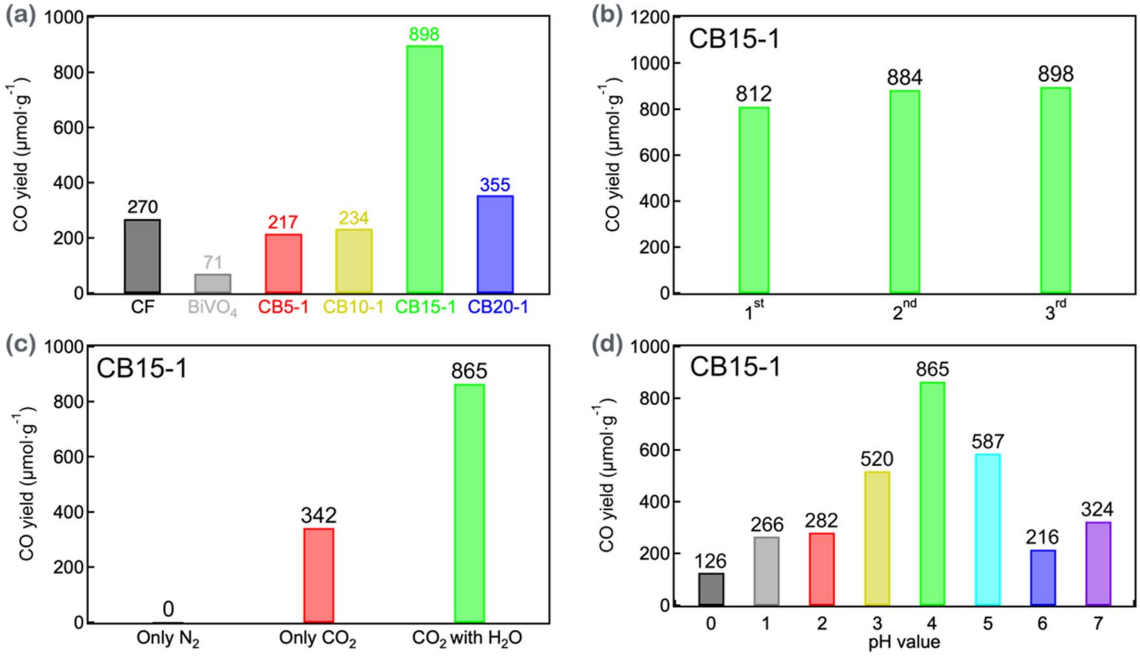

Fig. 5 The CO production yields of CF, $BiVO_4$ and CB heterojunction materials at one sun irradiation for 12 h. (a) The comparison of the CO yields of CF, $BiVO_4$, and CB heterojunction materials in varied proportions as indicated; (b) the reproducibility of CB15-1 showing the results of experiments three times; (c) the CO yields of CB15-1 under different conditions: only N_2 injection (no CO_2 and H_2O), no H_2O but with CO_2 only, and normal conditions with the presence of both CO_2 and H_2O; (d) the CO yields of CB15-1 with $BiVO_4$ synthesized at varied pH values.

resulting in a decrease in photocatalytic efficiency. This suggests that not only the ratio but also the specific interaction and surface area coverage between CF (nanocrystals) and $BiVO_4$ (bulky particles) are critical for forming efficient heterojunctions that enhance photocatalytic activity. Additionally, the reproducibility of CB15-1 is shown in Fig. 5b, with an average CO production yield of 865 ± 38 μmol g^{-1} for three measurements, demonstrating the good reproducibility of this heterojunction photocatalyst.

Furthermore, the photocatalytic performance of CB15-1 under different environmental conditions was studied. As shown in Fig. 5c, no CO was produced if only N_2 was injected (no CO_2 and H_2O) and low CO production yield was obtained if only CO_2 was injected (no H_2O). These control experiments demonstrated that both CO_2 and H_2O are needed for the photocatalytic CO_2 reduction to occur with great CO production yield. The first control experiment confirmed that the CO produced in the photocatalytic reaction originated from CO_2 reduction, not from the degradation of the catalyst itself. The experiment also verified the importance of water vapor in the photocatalytic system because effective photocatalytic cycling requires simultaneous CO_2 reduction and H_2O oxidation to avoid carrier accumulation. The results showed that CB15-1 effectively reduced CO_2 to CO in the presence of water vapor, highlighting its excellent catalytic activity and product selectivity.

The role of H_2O in the photocatalytic reaction is two fold: it serves as the electron donor for the oxidation reaction and ensures charge carrier balance by participating in the oxidation half-reaction. Without sufficient water vapor, the absence of an oxidation reaction leads to charge carrier accumulation, significantly increasing recombination rates and thereby inhibiting photocatalytic activity. This is evident from the decrease in CO yield to 342 μmol g^{-1} when H_2O was absent in the system. In contrast, introducing H_2O facilitates the formation of hydroxyl radicals or other intermediate species, sustaining the oxidation half-reaction and enabling efficient charge separation. These findings emphasize the critical role of water vapor in achieving high photocatalytic performance in the CF/$BiVO_4$ system.

Notably, the ability of Pb-based photocatalysts to achieve effective CO_2 reduction in the presence of water vapor marks a significant advancement, as pristine CF perovskites are typically sensitive to water, leading to structural degradation and reduced catalytic activity. The formation of the CF/$BiVO_4$ heterojunction not only stabilizes the CF perovskite but also allows it to function efficiently under water vapor conditions, mimicking real-world photocatalytic environments. This highlights the potential of the CF/$BiVO_4$ composite to address the inherent limitations of CF perovskites and make them viable for practical applications in CO_2 reduction systems.

Moreover, photocatalytic efficiency can be further optimized by adjusting the synthesis environment of $BiVO_4$, as the pH value significantly influences its surface properties and crystal structure, affecting carrier recombination rates and photocatalytic performance.[83] As shown in Fig. 5d, when the pH value during $BiVO_4$ synthesis ranged from 0 to 7, the photocatalytic efficiencies of the final composite material CB15-1 were 126, 266, 282, 520, 865, 587, 216, and 324 μmol g^{-1}, respectively. This indicated that the best heterojunction formed and the highest photocatalytic efficiency of CB15-1 was achieved when the pH was 4 during $BiVO_4$ synthesis. Due to the differing crystal lattice arrangements of various materials, when two materials are joined, a "lattice mismatch" occurs at the interface. This mismatch results in the interlocking of atoms and slight deformation of the crystal lattices.[84] However, if the degree of strain can be controlled, it is possible to manage the microstrain between the two materials. This control allows the formation of a more favorable internal electric field at the material interface, enhancing the rapid separation of electrons and holes, thereby increasing photocatalytic performance. Experiments showed that cubic phase aged CF and tetragonal phase $BiVO_4$ at pH 4 exhibited the best heterojunction and the highest photocatalytic efficiency, demonstrating the controllability of inter-crystalline strain within heterostructures.

The recyclability and long-term photocatalytic performance of CB15-1 were further evaluated to explore its stability and efficiency. As illustrated in Fig. S8,† the recyclability study showed that the CO production efficiencies for cycle 1, cycle 2, and cycle 3 were measured to be 812, 346, and 207 μmol g^{-1}, respectively. The observed decline in activity across cycles suggests that, while the composite can rejuvenate aged CF perovskites and provide significant initial photocatalytic performance, its long-term recyclability is hindered by the intrinsic instability of the CF component. Additionally, the long-term photocatalytic performance under continuous illumination was assessed, as shown in Fig. S9.† The CO yield exhibited a linear increase over 12 hours of reaction, with values of 240, 485, 569, 646, 685, and 812 μmol g^{-1} at intervals of 2, 4, 6, 8, 10, and 12 hours, respectively. This indicates that CB15-1 remains efficient and stable during extended illumination, highlighting its potential for practical applications within daily operational light cycles.

Table S5† was compiled to summarize the contributions of various heterostructure materials to photocatalytic experiments as reported in the literature. This highlights that the S-scheme heterojunctions reported herein are the most promising candidates for photocatalytic experiments in semiconductor materials. In particular, our CB-15 S-scheme heterojunction catalyst shows the best performance among the others for photocatalytic CO_2 reduction.

Conclusion

In conclusion, an S-scheme heterojunction between aged CF and $BiVO_4$ was successfully synthesized using the one-pot and stirring methods. The reaction conditions were optimized using the stirring method by adjusting the material ratios and modifying the pH value of $BiVO_4$. The formation of the heterostructure was confirmed through XRD, SEM-EDS, PL, TCSPC, and UPS spectral analyses. When the CF to $BiVO_4$ ratio was 15 : 1 and the synthetic $BiVO_4$ pH was set to 4, the CO production yield reached 865 ± 38 μmol g^{-1} in 12 h under one sun irradiation. This heterojunction exhibited excellent reproducibility and selectivity for photocatalytic products, with 100% CO selectivity. Compared to a single material reacting in a humid environment, the heterojunction showed significant enhancement (over a three fold increase compared to aged CF). This enhancement can be attributed to the effective charge separation within the S-scheme heterojunction, which inhibited electron–hole recombination and allowed more electrons to participate in the photocatalytic CO_2 reduction. The study not only successfully synthesized an S-scheme heterojunction but also revitalized the photocatalytic efficiency of aged perovskite materials, fundamentally addressing the issue of degradation in perovskites. This provides an effective approach for designing stable and high-performance photocatalysts in the future.

Data availability

The data supporting this article have been included as part of the ESI.†

Conflicts of interest

There are no conflicts of interest to declare.

Acknowledgements

We gratefully acknowledge the support of the National Science and Technology Council (NSTC), Taiwan (grant NSTC 112-2639-M-A49-001-ASP and NSTC 113-2639-M-A49-001-ASP) and the Center for Emergent Functional Matter Science of National Yang Ming Chiao Tung University (NYCU) from the Featured Areas Research Center Program within the framework of the Higher Education Sprout Project by the Ministry of Education (MOE) in Taiwan.

References

1 M. Graetzel, *Acc. Chem. Res.*, 2002, **14**, 376–384.

2 T. J. Meyer, *Acc. Chem. Res.*, 1989, **22**, 163–170.

3 A. J. Bard and M. A. Fox, *Acc. Chem. Res.*, 1995, **28**, 141–145.

4 D. Gust, T. A. Moore and A. L. Moore, *Acc. Chem. Res.*, 2009, **42**, 1890–1898.

5 Y. Tachibana, L. Vayssieres and J. R. Durrant, *Nat. Photonics*, 2012, **6**, 511–518.

6 R. Franke and C. Franke, *Chemosphere*, 1999, **39**, 2651–2659.

7 Y. Jinyu, W. Yayang, S. Xiaofang, L. Dongliang, R. Lu, Z. Yuan and L. Yuesheng, *J. Radiat. Res. Radiat. Process.*, 2023, **39**, 19–28.

8 Q. Wang, Z. Fang, W. Zhang and D. Zhang, *Adv. Fiber Mater.*, 2022, **4**, 342–360.

9 J. Cai, D. Li, L. Jiang, J. Yuan, Z. Li and K. Li, *Energy Fuels*, 2023, **37**, 4878–4897.

10 J. Chen, T. Li, X. An and D. Fu, *Energy Fuels*, 2024, **38**, 7614–7636.

11 F. Xu, K. Meng, B. Cheng, S. Wang, J. Xu and J. Yu, *Nat. Commun.*, 2020, **11**, 4613.

12 X. Deng, J. Zhang, K. Qi, G. Liang, F. Xu and J. Yu, *Nat. Commun.*, 2024, **15**, 4807.

13 C. Wehrenfennig, G. E. Eperon, M. B. Johnston, H. J. Snaith and L. M. Herz, *Adv. Mater.*, 2014, **26**, 1584–1589.

14 Z. Xiao, Y. Yuan, Q. Wang, Y. Shao, Y. Bai, Y. Deng, Q. Dong, M. Hu, C. Bi and J. Huang, *Mater. Sci. Eng., R*, 2016, **101**, 1–38.

15 J. Maes, L. Balcaen, E. Drijvers, Q. Zhao, J. D. Roo, A. Vantomme, F. Vanhaecke, P. Geiregat and Z. Hens, *J. Phys. Chem. Lett.*, 2018, **9**, 3093–3097.

16 A. K. Jena, A. Kulkarni and T. Miyasaka, *Chem. Rev.*, 2019, **119**, 3036–3103.

17 Y. Li, Z.-F. Shi, X.-J. Li and C.-X. Shan, *Chin. Phys. B*, 2019, **28**, 017803.

18 H. Wang, X. Wang, R. Chen, H. Zhang, X. Wang, J. Wang, J. Zhang, L. Mu, K. Wu and F. Fan, *ACS Energy Lett.*, 2018, **4**, 40–47.

19 J. Chen, J. Yin, X. Zheng, H. A. Ahsaine, Y. Zhou, C. Dong, O. F. Mohammed, K. Takanabe and O. M. Bakr, *ACS Energy Lett.*, 2019, **4**, 1279–1286.

20 A. F. Gualdron-Reyes, J. Rodriguez-Pereira, E. Amado-Gonzalez, P. J. Rueda, R. Ospina, S. Masi, S. J. Yoon, J. Tirado, F. Jaramillo, S. Agouram, V. Munoz-Sanjose, S. Gimenez and I. Mora-Sero, *ACS Appl. Mater. Interfaces*, 2020, **12**, 914–924.

21 S. Ito, S. Tanaka, K. Manabe and H. Nishino, *J. Phys. Chem. C*, 2014, **118**, 16995–17000.

22 J. A. Christians, P. A. M. Herrera and P. V. Kamat, *J. Am. Chem. Soc.*, 2015, **137**, 1530–1538.

23 B. Conings, J. Drijkoningen, N. Gauquelin, A. Babayigit, J. D'Haen, L. D'Olieslaeger, A. Ethirajan, J. Verbeeck, J. Manca and E. Mosconi, *Adv. Energy Mater.*, 2015, **5**, 1500477.

24 D. Bryant, N. Aristidou, S. Pont, I. Sanchez-Molina, T. Chotchunangatchaval, S. Wheeler, J. R. Durrant and S. A. Haque, *Energy Environ. Sci.*, 2016, **9**, 1655–1660.

25 N. J. Jeon, J. H. Noh, Y. C. Kim, W. S. Yang, S. Ryu and S. I. Seok, *Nat. Mater.*, 2014, **13**, 897–903.

26 R. Vidal, J.-A. Alberola-Borràs, S. N. Habisreutinger, J.-L. Gimeno-Molina, D. T. Moore, T. H. Schloemer, I. Mora-Seró, J. J. Berry and J. M. Luther, *Nat. Sustain.*, 2021, **4**, 277–285.

27 L. Protesescu, S. Yakunin, M. I. Bodnarchuk, F. Krieg, R. Caputo, C. H. Hendon, R. X. Yang, A. Walsh and M. V. Kovalenko, *Nano Lett.*, 2015, **15**, 3692–3696.

28 R. W. Epps, K. C. Felton, C. W. Coley and M. Abolhasani, *Lab Chip*, 2017, **17**, 4040–4047.

29 L. Protesescu, S. Yakunin, S. Kumar, J. Bär, F. Bertolotti, N. Masciocchi, A. Guagliardi, M. Grotevent, I. Shorubalko and M. I. Bodnarchuk, *ACS Nano*, 2017, **11**, 3119–3134.

30 Y. Wang, Y.-e. Shi, T. Li, H. Wang, Y. Li, Y. Xiong, S. Peng and Z. Wang, *Nanoscale Adv.*, 2019, **1**, 834–839.

31 N. Sitapure, T. Qiao, D. H. Son and J. S.-I. Kwon, *Comput. Chem. Eng.*, 2020, **139**, 106872.

32 S. S. Bhosale, E. Jokar, Y. T. Chiang, C. H. Kuan, K. Khodakarami, Z. Hosseini, F. C. Chen and E. W.-G. Diau, *ACS Appl. Energy Mater.*, 2021, **4**, 10565–10573.

33 S. S. Bhosale, S. Narra, E. Jokar, A. Manikandan, Y.-L. Chueh and E. W.-G. Diau, *J. Mater. Chem. C*, 2021, **9**, 17341–17348.

34 F. Cova, A. Erroi, M. L. Zaffalon, A. Cemmi, I. D. Sarcina, J. Perego, A. Monguzzi, A. Comotti, F. Rossi and F. Carulli, *Nano Lett.*, 2024, **24**, 905–913.

35 J. Shi, X. Xu, D. Li and Q. Meng, *Small*, 2015, **11**, 2472–2486.

36 J. M. Ball and A. Petrozza, *Nat. Energy*, 2016, **1**, 1–13.

37 S. Shrestha, *Methylammonium Lead Iodide Perovskite for Direct X-ray Detection*, Friedrich-Alexander-Universitaet Erlangen-Nuernberg, Germany, 2018.

38 S. Shao and M. A. Loi, *Adv. Mater. Interfaces*, 2020, **7**, 1901469.

39 Z. Fang, J. Sun, S. F. Liu and L. Ding, *J. Semicond.*, 2023, **44**, 080201.

40 K. S. Aleksandrov, *Ferroelectrics*, 1976, **14**, 801–805.

41 C. J. Howard and H. T. Stokes, *Acta Crystallogr., Sect. A: Found. Crystallogr.*, 2005, **61**, 93–111.

42 J. Hu, X. Xiong, W. Guan, Z. Xiao and H. Long, *Mater. Today Chem.*, 2022, **24**, 100792.

43 B. Diouf, A. Muley and R. Pode, *Energies*, 2023, **16**, 6498.

44 J. Yu and A. Kudo, *Adv. Funct. Mater.*, 2006, **16**, 2163–2169.

45 Y. Li, J. Wang, H. Yao, L. Dang and Z. Li, *J. Mol. Catal. A: Chem.*, 2011, **334**, 116–122.

46 Y. Wang, K. Deng and L. Zhang, *J. Phys. Chem. C*, 2011, **115**, 14300–14308.

47 J. Cao, B. Xu, B. Luo, H. Lin and S. Chen, *Catal. Commun.*, 2011, **13**, 63–68.

48 J. Tian, Y. Sang, G. Yu, H. Jiang, X. Mu and H. Liu, *Adv. Mater.*, 2013, **25**, 5075–5080.

49 Y. Zhou, Y. Zhang, M. Lin, J. Long, Z. Zhang, H. Lin, J. C.-S. Wu and X. Wang, *Nat. Commun.*, 2015, **6**, 8340.

50 A. Malathi, J. Madhavan, M. Ashokkumar and P. Arunachalam, *Appl. Catal., A*, 2018, **555**, 47–74.

51 L. Meng, Y. Qu and L. Jing, *Chin. Chem. Lett.*, 2021, **32**, 3265–3276.

52 W. Wang, X. Huang, S. Wu, Y. Zhou, L. Wang, H. Shi, Y. Liang and B. Zou, *Appl. Catal., B*, 2013, **134**, 293–301.

53 Z. He, Y. Shi, C. Gao, L. Wen, J. Chen and S. Song, *J. Phys. Chem. C*, 2014, **118**, 389–398.

54 W. Zhao, Y. Liu, Z. Wei, S. Yang, H. He and C. Sun, *Appl. Catal., B*, 2016, **185**, 242–252.

55 Y. Liu, J. Kong, J. Yuan, W. Zhao, X. Zhu, C. Sun and J. Xie, *Chem. Eng. J.*, 2018, **331**, 242–254.

56 W. Zhao, Y. Feng, H. Huang, P. Zhou, J. Li, L. Zhang, B. Dai, J. Xu, F. Zhu and N. Sheng, *Appl. Catal., B*, 2019, **245**, 448–458.

57 W. Wang, X. Feng, L. Chen and F. Zhang, *Ind. Eng. Chem. Res.*, 2021, **60**, 18384–18396.

58 X. Y. Yue, L. Cheng, J. J. Fan and Q. J. Xiang, *Appl. Catal., B*, 2022, **304**, 120979.

59 L. Yang, A. U. Pawar, R. P. Sivasankaran, D. Lee, J. Ye, Y. Xiong, Z. Zou, Y. Zhou and Y. S. Kang, *J. Mater. Chem. A*, 2023, **11**, 19172–19194.

60 A. H. Bhosale, S. Narra, S. S. Bhosale and E. W.-G. Diau, *J. Phys. Chem. Lett.*, 2022, **13**, 7987–7993.

61 O. A. Arotiba, B. O. Orimolade and B. A. Koiki, *Curr. Opin. Electrochem.*, 2020, **22**, 25–34.

62 W. Zhang, A. R. Mohamed and W. J. Ong, *Angew. Chem., Int. Ed.*, 2020, **59**, 22894–22915.

63 Y. Bao, S. Song, G. Yao and S. Jiang, *Sol. RRL*, 2021, **5**, 2100118.
64 J. Li, P. Tu, Q. Yang, Y. Cui, C. Gao, H. Zhou, J. Lu and H. Bian, *Sci. Rep.*, 2024, **14**, 10643.
65 S. S. Bhosale, A. K. Kharade, S. Narra, S.-m. Chang and E. W.-G. Diau, *ACS Energy Lett.*, 2022, **8**, 280–288.
66 A. Yi, S. Chae, H. M. Luong, S. H. Lee, H. Lee, H. Yoon, D.-H. Kim, H. J. Kim and T.-Q. Nguyen, *Joule*, 2024, **8**, 2087–2104.
67 W.-J. Xu, Z.-Y. Du, W.-X. Zhang and X.-M. Chen, *CrystEngComm*, 2016, **18**, 7915–7928.
68 Z.-G. Li, M. Zacharias, Y. Zhang, F. Wei, Y. Qin, Y.-Q. Yang, L.-C. An, F.-F. Gao, W. Li and J. Even, *ACS Energy Lett.*, 2023, **8**, 3016–3024.
69 J. I. Langford and A. J. C. Wilson, *J. Appl. Crystallogr.*, 1978, **11**, 102–113.
70 G. F. Harrington and J. Santiso, *J. Electroceram.*, 2021, **47**, 141–163.
71 D. V. Talapin, A. L. Rogach, M. Haase and H. Weller, *J. Phys. Chem. B*, 2001, **105**, 12278–12285.
72 N. T. Thanh, N. Maclean and S. Mahiddine, *Chem. Rev.*, 2014, **114**, 7610–7630.
73 J. T. DuBose, A. Christy, J. Chakkamalayath and P. V. Kamat, *ACS Mater. Lett.*, 2021, **4**, 93–101.
74 Z. Wang, W. Luo, S. Yan, J. Feng, Z. Zhao, Y. Zhu, Z. Li and Z. Zou, *CrystEngComm*, 2011, **13**, 2500–2504.
75 S.-H. Chen, Y.-S. Jiang and H.-y. Lin, *ACS Omega*, 2020, **5**, 8927–8933.
76 P. Liu, W. Chen, W. Wang, B. Xu, D. Wu, J. Hao, W. Cao, F. Fang, Y. Li and Y. Zeng, *Chem. Mater.*, 2017, **29**, 5168–5173.
77 F. Zhang, H. Zhong, C. Chen, X.-g. Wu, X. Hu, H. Huang, J. Han, B. Zou and Y. Dong, *ACS Nano*, 2015, **9**, 4533–4542.
78 T. Tran-Phu, Z. Fusco, I. Di Bernardo, J. Lipton-Duffin, C. Y. Toe, R. Daiyan, T. Gengenbach, C.-H. Lin, R. Bo and H. T. Nguyen, *Chem. Mater.*, 2021, **33**, 3553–3565.
79 J. Tauc, R. Grigorovici and A. Vancu, *Phys. Status Solidi B*, 1966, **15**, 627–637.
80 P. Kubelka and F. Munk, *Z. Tech. Phys.*, 1931, **12**, 259–274.
81 Y. Yamada, T. Nakamura, M. Endo, A. Wakamiya and Y. Kanemitsu, *J. Am. Chem. Soc.*, 2014, **136**, 11610–11613.
82 S. Narra, P.-S. Liao, S. S. Bhosale and E. W.-G. Diau, *Nanomaterials*, 2023, **13**, 1718.
83 A. P. Zhang, J. Z. Zhang, N. Y. Cui, X. Y. Tie, Y. W. An and L. J. Li, *J. Mol. Catal. A: Chem.*, 2009, **304**, 28–32.
84 A. Sabbah, I. Shown, M. Qorbani, F.-Y. Fu, T.-Y. Lin, H.-L. Wu, P.-W. Chung, C.-I. Wu, S. R. M. Santiago and J.-L. Shen, *Nano Energy*, 2022, **93**, 106809.